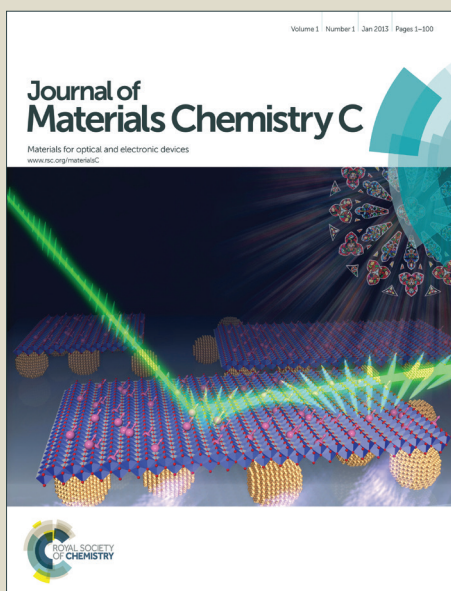


Journal of Materials Chemistry C

Accepted Manuscript



This is an *Accepted Manuscript*, which has been through the Royal Society of Chemistry peer review process and has been accepted for publication.

Accepted Manuscripts are published online shortly after acceptance, before technical editing, formatting and proof reading. Using this free service, authors can make their results available to the community, in citable form, before we publish the edited article. We will replace this *Accepted Manuscript* with the edited and formatted *Advance Article* as soon as it is available.

You can find more information about *Accepted Manuscripts* in the [Information for Authors](#).

Please note that technical editing may introduce minor changes to the text and/or graphics, which may alter content. The journal's standard [Terms & Conditions](#) and the [Ethical guidelines](#) still apply. In no event shall the Royal Society of Chemistry be held responsible for any errors or omissions in this *Accepted Manuscript* or any consequences arising from the use of any information it contains.

Structural Evolution and Carrier Scattering of Si Nanowires as a Function of Oxidation Time

Jung min Bae¹, Woo-Jung Lee^{1,3}, Jin won Ma¹, Jung hun Kim¹, Seung hoon Oh¹, Mann-Ho Cho^{1,*}, Kang chul², Seonghoon Jung⁴, Jaehun Park⁴

¹*Department of Physics and Applied Physics, Yonsei University, Seoul 120-749, Korea*

²*Advanced Photonic Research Institute, Gwangju Institute Science and Technology, Gwangju 500-712, Korea*

³*Electronics and Telecommunications Research Institute, 218 Gajeongno, Yuseong-gu, Daejeon 305-700, Korea*

⁴*Pohang Accelerator Laboratory, Pohang University of Science and Technology, Pohang, 790-784, Korea*

ABSTRACT

We investigated the morphological characteristics of the cross-sectional shape of Si-core nanowires (NWs) as a function of oxidation time. In the case of as-grown Si NWs, the Si cores were hexagons with a 3-fold symmetry, not a 6-fold symmetry, and this shape was transformed into a triangular shape with rounded edges after thermal oxidation. Structural changes in the cross section of the Si-core NWs were related to the surface free energy. Moreover, the morphological change in the oxide shell during the oxidation treatment suggested that the stress relaxation process is closely related with the structural evolution of the Si core. The change in defect states generated in Si/SiO₂ core/shell NWs during structural evolution was investigated by low-temperature photoluminescence and optical pump-THz probe spectroscopy measurements. In particular, surface defect states formed in the interfacial region between the Si core and the oxide shell were reduced during the oxidation process. Appropriate control of the surface state affected carrier scattering: the relaxation time of photogenerated carriers was significantly increased due to the reduction in surface defects.

1. Introduction

An advantage of Si over other semiconductor materials lies in its thermally grown oxide, SiO₂, since electrically active defects can be passivated by hydrogen to a much lower density, where their influence on the electrical properties of devices is minimal^{1,2}. Recently, Si NWs and oxidized Si NWs have also received considerable attention as building blocks for nanoelectronic devices and for use in chemical and biological sensors³⁻⁵. Numerous studies in recent decades have reported on the electrical properties of Si/SiO₂ core/shell structures with the goal of utilizing Si NWs in Si-based devices⁶⁻⁹. In addition, the mechanism responsible for the oxidation of Si NWs is an area of interest for researchers studying low-dimensional systems. Generally, in bulk Si, the oxidation kinetics can be adequately explained using the Deal-Grove model¹⁰. In Si NWs, the oxidation kinetics have also been interpreted using a Deal-Grove model that is modified slightly to have a linear-parabolic shape, to reflect the fact that the rate of oxidation of NWs is initially faster than the bulk oxidation rate, and gradually decreases due to the stress effect of the SiO₂ shell arising from the geometry of the convex wire^{6,8}. In contrast to conventional Si-based devices, NWs-based optoelectronic devices such as photodetectors, light-emitting diodes, and transistors have unique optical and electrical properties that arise from differences in their geometry^{7,9,11,12}. Generally, such properties can be explained simply by the high surface-to-volume ratio of NWs; in essence, the surface states of nanostructures are sufficiently numerous that they play a significant role in device properties. Especially, mobility is significantly affected by surface scattering: increased scattering at the wire surface lowers the mobility¹³. In cases where Si NWs are used for device channels, the shape of the Si core is also a key determinant of carrier lifetime and mobility, etc. However, although device characteristics are significantly affected by the shape of the Si core and by interfacial defects between the Si core and the SiO₂ shell, in-depth fundamental studies of the above phenomena

have not yet been reported.

In this study, we investigated the evolution of the cross-sectional geometry of Si-core NWs and their defect states as a function of oxidation time using transmission electron microscopy (TEM) and low-temperature photoluminescence (LTPL), respectively. Si NWs were grown using a vapor–liquid–solid method; most of the NWs grew in the [111] direction and had hexagonal cross sections with a 3-fold symmetry, rather than a perfect 6-fold symmetry. Based on structural changes of the Si core observed after various durations of an oxidation treatment, we propose a schematic model to explain the stress effect, and calculate the initial diameter of a 3-fold symmetrical hexagonal Si core. Strong stress was typically generated at the interface between the Si core and the SiO₂ shell due to the configurational shape of the NWs and the volume expansion of Si to SiO₂ as a result of oxidation^{14,15}. We discovered that a distinct PL signature is generated in oxidized Si NWs, corresponding to the oxygen vacancy of twofold-coordinated silicon lone pair centers (O-Si-O) that are present near the Si band gap. In the case of NWs, it is well known that the carriers that are photoexcited by Optical pump THz Probe (OPTP) spectroscopy can be easily trapped at the surface in inverse proportion to wire diameter, resulting in a rapid decay of carrier lifetime^{16,17}. However, notably, the carrier relaxation times of oxidized Si NWs, as determined using a specialized analysis for detecting ultrafast carrier dynamics on the picosecond time scale, were increased slightly despite the decreasing diameter of the Si core as the oxidation treatment proceeded; this indicates that the decrease in surface defects with increasing oxidation time also affects the carrier relaxation time. This comprehensive research on oxidized Si NWs provides helpful information for nanoscale device industry for use in the not-too-distant future.

I. EXPERIMENT

Si NWs were synthesized on a clean Si (111) substrate by means of a vapor–liquid–solid method with a Au catalyst, using an ultrahigh-vacuum chemical vapor deposition system. Experimental conditions for wire growth have been described in detail in a previous report¹⁸. Si NWs were vertically grown over a period of up to 30 min at 600 °C by filling the deposition chamber with a mixture of SiH₄ gas (10 sccm) as the precursor and H₂ gas (200 sccm) as the carrier gas, with the pressure maintained at 0.05 torr by a feedback system using a throttle valve and a baratron gauge; these conditions for the vertical growth of Si NWs were as required by our system¹⁹. Si NWs with a mean length of approximately 2.5 μm Si NWs were controlled by the growth time. The morphological and crystalline characteristics of Si NWs were individually analyzed by field emission scanning electron microscopy (FE-SEM, JSM 6500F, Jeol) and field emission TEM (Tecnai F20), as shown in Fig. 1a. The resulting Si NWs contained a large number of Au nanoparticles (2–3 nm) on the wire sidewalls (Fig. 1b). The majority of the Si NWs grew in the [111] growth direction, as verified by a selective area electron diffraction (SAED) analysis (Fig. 1b). Their average diameter was 82.5 nm with a standard deviation of ±16 nm (Fig. 1c). In the case of the thermal oxidation of a Si NW with an Au tip, oxidation processes in both the radial and axial directions can occur at the Si/Au interface²⁰. In this experiment, to avoid interactions between Au and Si during the thermal oxidation, Au particles were removed from the NWs prior to the oxidation process by etching using a KI-I₂ solution. The morphologies of Si NWs with and without Au atoms were measured by both high-resolution TEM and scanning TEM at 200 kV (Fig. 1d, **Supporting Figures S1a and S1b**), allowing us to verify that the Au had been completely removed from the nanoparticles.

Thermal oxidation experiments on Si NWs were performed for various lengths of time,

using a tube zone furnace operated at 900 °C and with a constant oxygen gas flow of 10 sccm. First, to avoid pre-oxidation, air was evacuated from the furnace by means of a pump and the chamber was then refilled with 1 atm of Ar and heated to the experimental oxidation temperature of 900 °C. Upon reaching this temperature, the oxidation was initiated by switching the gas from Ar to O₂; the Si NWs were then oxidized for 30 min, 1 h, 2 h, or 9 h. To stop the oxidation reaction, the gas flow was quickly switched back to Ar gas and the furnace was allowed to cool down. The exact SiO₂ shell thickness and morphology were investigated using both high-resolution TEM mode and scanning TEM mode at 200 kV. To investigate the crystal structure and cross-sectional shapes of the oxidized Si cores, oxidized NWs were individually cut using a focused ion beam (FIB, Quanta 3D, FEI). Their chemical structure was examined by X-ray photoelectron spectroscopy (XPS) using a monochromatic Al K α (1486.6 eV) source. Defect states on NWs were measured by LTPL using a He-Cd laser (325 nm) as an excitation source, in a cooling system using a closed-cycle liquid helium cryogenerator (7 K). The influence of the NW surface defects was investigated by measuring the relaxation time of photoexcited carriers using OPTP tools. The second harmonic (400 nm, 3.1 eV) of an amplified laser through a type-II β -Barium Borate (BBO) crystal was used as the pump beam. THz probe pulse was generated via optical rectification of the fundamental pulse in a 10 x 10 mm <110> ZnTe crystal of thickness 1 mm^{21,22}. After an ultrafast optical pump beam (400 nm) excited the free carriers in the NWs, the transient change of the NWs in the frequency range of 0.2 THz to 2.6 THz was probed by THz pulses. The time evolution of the pump-probe signal was collected by scanning the time delay of the pump pulses relative to the THz pulse.

II. Results and discussion

The evolving morphology of Si NWs during their oxidation was studied by TEM analysis of cross sections of a series Si NW samples that had undergone a thermal oxidation treatment process for different lengths of time (Fig. 2). TEM analyses verified that the Si NWs were transformed into a Si/SiO₂ core/shell structure. As the oxidation time was increased, the SiO₂ shell increased in thickness and the diameter of the Si core decreased; after 9 h of thermal oxidation, the Si core disappeared and a NW composed of only SiO₂ was formed (**Supporting Figure S1c–f**). Interestingly, our Si NWs grown in the [111] direction had hexagonal cross sections with a 3-fold symmetry (Figs. 2a, 2e), which is not consistent with theoretical results, which indicate a 6-fold symmetry²³. Based on the Si NW with 3-fold symmetry, the oxidation process was further examined. The cross-sectional shape of the SiO₂ shell was initially similar to the shape of the Si core: hexagonal with a 3-fold symmetry. However, as the oxidation progressed, the cross-sectional shape of the Si core became more triangular. The long side became relatively longer and the short side became relatively shorter, while maintaining a 3-fold symmetry; this resulted in a triangular shape with rounded edges. With further oxidation, the SiO₂ shell eventually changed to a circular shape, due to volume expansion caused by the high temperature used in the oxidation process.

We verified the cross-sectional crystal structure of the Si core through SAED analysis; all side directions in the hexagonal shaped material had {112} facets (**Supporting Figure S2**). The cause of the 3-fold symmetry in Si core NW can be attributed to fluctuations in the Au catalyst during wire growth, which is known to induce faceting on Si (111) and (001) surfaces^{24,25,26}. In the case of the initial crystallization of Si atoms in the Au catalyst during NW growth, step-edges form on the Si substrate due to surface reconstruction, providing sites for atomic incorporation and nucleation; that is to say, a faceting transition develops with

continuous changes in step density and interactions between the steps²⁷. The thermodynamically stable state of the Si (111) substrate has a faceted crystallographic symmetry, which is relevant to the orientational phase diagram in which the step formation energy on the Si surface is orientationally stable along the $[\bar{1}\bar{1}2]$ direction²⁸. Thus, Au can determine the specific facets $\{112\}$ of the Si core NW, which is consistent with our Si NWs. The deposited Si monolayer can become faceted to lower the total energy, and the initial cross-sectional shape of the Si can be determined by the Au boundary conditions (Fig. 3a). Moreover, several reports have shown that the Si NWs with a cross-sectional shape with a 3-fold symmetry were grown in the chamber system based on UHV-CVD^{28,29,30}. These Si NWs possessed faceted sidewalls with a sawtooth arrangement, near equilibrium, which is because growth occurs via the most energetically favorable facet, revealing balanced alternate facets²⁸. This faceting phenomenon on sidewalls was also observed in our Si NW³¹. Based on these considerations, it appears that a crystal structure with a 3-fold symmetry is the stable state in a UHV environment during the growth of Si NW. All of the as-grown Si NWs revealed cross-sections with a 3-fold symmetry in various diameters ranging from ~ 40 nm to ~ 160 nm as displayed in **Supporting Figure S3**.

Next, to investigate the evolution of the Si NWs during the oxidation process, we attempted to calculate the initial diameter based on a hexagonal Si core with a 3-fold symmetry (Fig. 3b). Assuming an asymmetric hexagon, the Si core diameter measured from the TEM image of Fig. 1b can be determined based on the $[112]$ direction, which corresponds to the length 'D' shown as a white arrow in Fig. 3a. Using the short and long side lengths of 'X' and 'Y', respectively, it is possible to determine the length of D as follows: $X + Y = D$. Defining η as the ratio Y/X , the hexagonal area is given by $A = \frac{\sqrt{3}}{4}(1 + 4\eta + \eta^2)X^2$ and A is thus calculated to be

approximately $0.64D^2$. The value for η can be measured from TEM images of individual Si NWs, and was determined to have a mean value of 1.535 and standard deviation of 0.068 (Figs. 3c, 3d). Although the diameters of the Si NWs vary widely from 40 to 160 nm, their η ratios all tend to be quite close to 1.5 regardless of diameter. Thus, we propose that the hexagonal shape with 3-fold symmetry and with shape characterized by a value of η of approximately 1.5 is the most stable shape for a growth temperature of 600 °C, which resulted from the lowest surface energy of Si atoms in the Au catalyst.

The shape of the SiO₂ shell surrounding the Si core gradually changes with increasing shell thickness, eventually assuming a circular shape. During the oxidation process, the lengths X and Y both decreased with the same value, while maintaining a 3-fold symmetry (Figs. 2b, 2f). As the thermal oxidation process continued, the shape of the Si core evolved into a triangle with rounded edges; that is, the short side was transformed into a rounded edge of the Si core (Figs. 2c, 2g). Eventually, this triangular shape gradually changed into a circular shape as the Si core shrank to a very small size (Fig. 2h). We systematically explain this change in shape by using the geometrical and mathematical illustration of Fig. 4; a more detailed mathematical description of the process is given in the Appendix. Defining r as the radius of the oxidized SiNW with a circular SiO₂ shell due to the volume expansion at the endpoint of the thermal oxidation, as observed for oxidized samples, r can be related to A and A_δ as in the following equation.

$$r^2 = (1/\pi)(2.2A - 1.2A_\delta) \quad \text{----- (i)}$$

where, A is the area of the as-grown SiNW and A_δ is the area of Si core NW after oxidation. Moreover, we can confirm that the mean η value of 1.535 (recall Fig. 3c) is reliable. The above equation can provide information on the initial Si core diameter 'D' before the thermal oxidation by substituting the figures of 2r and D_δ measured from the individual oxidized Si

NWs (Fig. 4b). The initial Si core diameters were extracted from the TEM images of oxidized Si NWs given in Fig. 2 using the above equation, yielding initial sizes of about 96 nm (Fig. 2a–d) and 75 nm (Fig. 2e–h). Interestingly, as adjacent short sides in the 3-fold hexagon decrease below a value for X_δ value of 10 nm (as calculated from Eq. (3) in the Appendix) during the oxidation process, the hexagonal shape becomes transformed into a triangular shape with three rounded edges. As the oxidation process continues, this shape is maintained and Y_δ (the long side) gradually decreases as evidenced by the cross-sectional shape. To show this more clearly, Fig. 5 illustrates the evolution of the Si in the cross-sectional shape of a core for oxidation times from 30 min to 2 h.

From the above the equations, the initial diameters of oxidized Si NWs can be obtained as a function of oxidation time; **Supporting Table S1** summarizes these diameters, showing good agreement with our experimental results (Fig. 1c). The SiO₂ shell thicknesses formed on the Si NWs were measured at various oxidation times, and are shown graphically in Fig. S4. Figure 6a shows the Si core diameters and total diameters of Si/SiO₂ core/shell NWs at various oxidation times, showing that the oxidation was very rapid during approximately the first hour, and then slowed, finally becoming saturated. The change in SiO₂ shell thickness as a function of oxidation time was compared with the modified Deal-Grove curve as indicated in Fig. S4.
^{10,32} The measured oxidation rate agrees well with a slightly modified Deal-Grove curve : that is to say, the oxidation rate was initially faster than that for a planar Si substrate because the exposed convex surfaces of the Si NWs were wider than the planar interface of Si/SiO₂. As the oxidation continued, its rate decreased due to the limitations of the convex geometry⁸. We quantitatively derived the volume of the SiO₂ shell and of the interfacial area between the Si core and the SiO₂ shell as a function of oxidation time from Si NWs with calculated initial diameter of 80 nm (Fig. 6b); the results indicated that the volume of the SiO₂ shell increased

while the interfacial area between the Si core and SiO₂ shell decreased with increasing oxidation time.

The oxidation of Si NWs inevitably induces stress due to the volume expansion of the SiO₂ shell^{14,15}. The induced stress is evident from the changes in TEM images of the Si cross section (Fig. 2b and Fig. S2a): the three long sides of the 3-fold symmetrical hexagon become slightly dented due to the formation of the SiO₂ shell. Moreover, the shape of the oxide shell is dependent on the shape of the Si core: the SiO₂ shell becomes rounded and then changes to a circular shape as the shape of the core Si is transformed into a triangular shape with round edges. To investigate the stress component in the Si core with a 3-fold symmetrical hexagonal shape, we considered the use of the stress mapping method conducted on cylindrical Si NWs¹⁴. Different types of stress appear to be generated in the Si core and the SiO₂ shell: (i) in the SiO₂ shell, compressive stress is induced along the perpendicular direction, while tensile stress is induced along the direction parallel to the interface of Si/SiO₂, and (ii) in the Si core, compressive stress is induced along both the perpendicular and the parallel directions to the interface of the Si/SiO₂. In the SiO₂ shell, both stresses weaken with increasing distance from the Si core. Since the strength of the stress of the SiO₂ shell can be determined by its viscosity, a cross section of a SiO₂ shell with a 3-fold hexagon is transformed into a circular shape by volume expansion under the high oxidation temperature through a stress relaxing process³³. On the other hand, if the oxidation temperature is not sufficiently high, the SiO₂ shell is unlikely to change its shape by volume expansion; in this case, the stress is not relaxed. Our data on the evolution of SiO₂ from a hexagonal to a circular shape indicated that the stress was completely in the case of an oxidation time of 2 h at 900 °C. A schematic diagram illustrating the stress component is given in **Supporting Figure S5**.

We investigated defect states that arise during the oxidation process, such as oxygen

vacancies, because carrier mobility on the NW surface is significantly affected by defects, which induce carrier scattering¹⁶. To investigate defect states, the surface chemical states on oxidized Si NWs were investigated as a function of oxidation time using XPS (**Supporting Figure S6**). In the XPS spectra for the Si 2*p* core-level, various SiO_x defect states of Si¹⁺, Si²⁺ and Si³⁺ were observed, which are caused by the formation of native oxides (Fig. S6a)³⁴. We also performed Ne ion sputtering on the oxidized Si NW to collect information on the interfacial state between the Si core and the SiO₂ shell (Fig. S6b). SiO_x states began to appear with increasing sputtering time. After sputtering for 25 min, the SiO₂ shell was completely removed and the SiO_x state also disappeared, showing that the defect states were dominantly distributed at the interface between the Si core and the SiO₂ shell.

Although the interfacial SiO_x state was measured in the XPS depth profiling, it does not exactly reflect the defect states that arise from physical damage to the oxide layer during the sputtering process. To verify the presence of oxygen vacancies in oxidized Si NWs without any external physical damage, LTPL measurements at 7 K were carried out on samples exposed to various oxidation times (Fig. 7a). In the case of as-grown Si NWs, a broad peak near 522 nm appeared, arising from neutral oxygen vacancies ($\equiv\text{Si}-\text{Si}\equiv$) in the native oxide³⁵. After a thermal oxidation, two main peaks at around 500 and 400 nm were observed in PL spectra of all oxidized Si NWs. The peak near 500 nm is considered to correspond to neutral oxygen vacancies, similar to that of the as-grown Si NWs, but slightly blue-shifted in proportion to oxidation time as a result of the decreasing diameter of the Si core. The peak around 400 nm is caused by oxygen vacancies near the Si band gap; the corresponding bond is a twofold-coordinated silicon lone pair center (O-Si-O)³⁵. This result demonstrates that the species of defect states formed by native oxides and thermal oxides can be clearly distinguished from one another. Furthermore, the spectra show a decrease in the PL intensities of the two peaks with

oxidation time, indicating a reduction in defect states. The PL peak for Si NWs oxidized for 9 h was significantly decreased, resulting from the full oxidation to form SiO₂ NWs, with no remaining Si/SiO₂ interfaces or their associated defect states.

Finally, we extracted the carrier relaxation time of the Si NWs as a function of oxidation time using OPTP measurements, a technique that is sensitive to surface defect states in nanostructures. The time-resolved THz spectrometer used for OPTP measurements is schematically shown in Fig. 8a. The relative change in the Si NWs with increasing oxidation time from 0 min to 2 h in the transmission of the THz pulse, $\Delta T/T_0$, was monitored as a function of time delay. To provide a more quantitative analysis, the normalized $\Delta T/T_0$ signal was fitted using two exponential decay functions (Fig. 8b). The fast carrier decay time, τ_1 , corresponds to intervalley scattering in the conduction band, because energized electrons may be scattered into side valleys on the subpicosecond time scale³⁶. The slower carrier decay time, τ_2 , is related to an interband transition, such as due to the cooling of the electrons in the initial state³⁶. Table 1 summarizes the two decay times (τ_1 and τ_2) collected for Si NWs that had been oxidized for various periods of time. The measured value of τ_1 was significantly increased while τ_2 was slightly increased with increasing oxidation time. The τ_1 reflecting intervalley scattering, was increased by a factor of two notably after an oxidation process of 30 min, and then became saturated with oxidation time. This implies that τ_1 is significantly increased with the reduction of the Si core of the NW during oxidation, resulting from a change in the conduction band of Si by the stress that is induced by SiO₂ formation. In contrast to that of bulk Si, a typical value for τ_2 for NWs is on the order of several hundreds of picoseconds due to its extremely large relative surface area. The reported relationship between τ_2 and wire diameter (d) complies with $\tau_2 \sim D^2$, then a decrease in wire diameter induces a decrease in the carrier decay time^{16,37}. However, τ_2 remained similar herein despite the decreasing D . This can be explained by the surface defect

states of the as-grown Si NWs and oxidized Si NWs. For as-grown Si NWs, τ_2 is primarily determined by surface defects induced by the native oxide, whereas after the oxidation, τ_2 is determined by the SiO₂/Si interfacial defects, i.e., we suggest that the reason for the increase of τ_2 after oxidation is the curing of surface defect states during the oxidation process despite the decreasing D . Therefore, it can be concluded that the reduction in D due to the oxidation of the Si surface was accompanied by a decrease in the density of SiO₂/Si interfacial defects, accounting for the similarity in the values for τ_2 despite the differences in d . This result indicates that the reduction in defect states resulting from surface passivation is an important factor in improving carrier mobility in nanoscale structures.

III. Conclusions

We investigated the change in the cross-sectional shape of Si-core NWs as a function of oxidation time. In as-grown Si NWs, the Si cores had a 3-fold symmetrical hexagonal cross sections. As the oxidation time was increased up to 2h, the cross-sectional shape of the Si core evolved to a triangular shape with rounded edges. We propose a schematic model of the Si core with a 3-fold hexagonal symmetry to explain the stress effect resulting from the volume expansion of SiO₂, and to calculate the initial diameter of the Si NW before the oxidation process, yielding results that were in agreement with the experimental results for all oxidation times studied, from 30 min to 9 h. From PL spectra, we were able to distinguish the defect states of native oxides and of thermal oxides. As-grown Si NWs contain neutral oxygen vacancies ($\equiv\text{Si}-\text{Si}\equiv$) in their native oxide, and oxidized Si NWs contain twofold-coordinated silicon lone pair centers (O-Si-O) at the Si/SiO₂ interface. OPTP measurements showed that the carrier relaxation times of the Si NWs increased slightly with increasing oxidation time, indicating that τ_1 and τ_2 can be affected by the degree of stress and the surface states at the SiO₂/Si interface, respectively, and showing that the control of the surface states in nanoscale

structures is an important factor in terms of improving carrier mobility in nanoscale devices.

Appendix

Two lines ‘ ρ ’ perpendicular to the sides X and Y can be drawn to meet point M on \overline{OF} , and straight lines \overline{LM} and \overline{MN} parallel to X and Y can then be drawn from M as expressed by a violet color in Fig. 4a. The two right-angled congruent triangles $\triangle EFM$ and $\triangle GFM$ are formed with the common hypotenuse of \overline{FM} , as depicted in the magnified image at the top of Fig. 4a. Because \overline{EF} and \overline{FG} have the same length, denoted hereafter as ‘ δ ’, δ has the range $0 \leq \delta \leq x$ (short side) and $0 \leq \delta \leq y-x$ (long side), where $X=2x$ and $Y=2y$. The length δ increases to x and y as the point M moves from F to O. Two lines perpendicular to each side of X and Y at their center points are drawn, and they contact each other at the center of the hexagon, as displayed in the sky-blue region. Using the geometry of a 3-fold symmetry hexagon, a regular triangle (dark grey) can be drawn at the center of the hexagon. Considering that half of \overline{LM} is ‘ $x-\delta$ ’ and that half of \overline{MN} is ‘ $y-\delta$ ’, which are defined as $x_\delta = x-\delta$ and $y_\delta = y-\delta$, respectively, one side of this regular triangle can be determined to have the length $Y-X$. Assuming that, after sufficient thermal oxidation, a SiO_2 shell forms in the shape depicted by the black circle, having radius r , the lengths X and Y of the grey hexagon shrink to lengths X_δ and Y_δ of the dark blue hexagon as shown in Fig. 4b. The distance between the outermost two edges of the Si core is defined as D_δ . The area of the Si core is A_δ , and the ratio Y_δ/X_δ is defined as η_δ . The area of the Si core before and after thermal oxidation can then expressed with the equations (1) and (2), respectively.

$$A = 3^{1/2}(1+4\eta + \eta^2)x^2 \quad \text{----- (1)}$$

$$A_\delta = 3^{1/2}(1+4\eta_\delta + \eta_\delta^2)x_\delta^2 \quad \text{----- (2)}$$

The Si atoms react with the O_2 gas supplied during the oxidation process, resulting in Si/SiO_2

core/shell NWs. The molecular volume of the SiO₂ shell is 2.2 times that of the Si core; considering this volume expansion, r can be obtained from the following equation.

$$2.2(A-A_{\delta})=\pi r^2-A_{\delta} \quad \text{----- (3)}$$

D can be expressed in terms of x and η (eq. 4), and D_{δ} can be also related to x_{δ} and η_{δ} (eq. 5) as follows.

$$D = X+Y = 2(x+y) = 2x(1+\eta) \quad \text{----- (4)}$$

$$D_{\delta} = X_{\delta}+Y_{\delta} = 2(x_{\delta}+y_{\delta}) = 2x_{\delta}(1+\eta_{\delta}) \quad \text{----- (5)}$$

By using the relations of $D_{\delta}=D-4\delta$, eq.(4) and eq. (5), the η and η_{δ} can be written as follows.

$$\eta_{\delta} = (x/(x-\delta))(\eta-1)+1 \quad \text{----- (6)}$$

Consequently, we can extract the initial diameter of the wire ‘ D ’ using the measured r , D_{δ} from the TEM images and η of 1.535.

ACKNOWLEDGEMENTS

This work was partially supported by IT R&D program of MKE/KEIT (Development of novel 3D stacked devices and core materials for the next generation flash memory), the Development of 25% Efficiency Grade Tandem CIGS Thin Film Solar Cell Core Technology (B551179-12-01-00) of the Ministry of Knowledge Economy and the Korea Research Council for Industrial Science and Technology of the Republic of Korea and the Industry–Academy joint research program between Samsung Electronics–Yonsei University.

References

1. M. Schulz, *Surface Science* **1983**, 132, 422.
2. F. J. Grunthaner and P. J. Grunthaner, *Material Science Reports* **1986**, 1, 65.
3. Y. Cui, Z. H. Zhong, D. L. Wang, W. U. Wang and C. M. Lieber, *Nano Lett.* **2003**, 3, 149.
4. X. F. Duan, C. M. Niu, V. Sahi, J. Chen, J. W. Parce, S. Empedocles and J. L. Goldman, *Nature* **2003**, 425, 274.
5. Y. Cui, Q. Q. Wei, H. K. Park and C. M. Lieber, *Science* **2001**, 293, 1289.
6. C. C. Buttner and M. Zacharias, *Appl. Phys. Lett.* **2006**, 89, 263106.
7. D. P. Yu, Z. G. Bai, J. J. Wang, Y. H. Zou, W. Qian, J. S. Fu, H. Z. Zhang, Y. Ding, G. C. Xiong, L. P. You, J. Xu and S. Q. Feng, *Phys. Rev. B* **1999**, 59, R2498.
8. D. Shir, B. Z. Liu, A. M. Mohammad, K. K. Lew and S. E. Mohnney, *J. Vac. Sci. Technol. B* **2006**, 24, 1333.
9. B. Z. Liu, Y. F. Wang, T. T. Ho, K. K. Lew, S. M. Eichfeld, J. M. Redwing, T. S. Mayer and S. E. Mohnney, *J. Vac. Sci. Technol. A* **2008**, 26, 370.
10. B. E. Deal and A. S. Grove, *J. Appl. Phys.* **1965**, 36, 3770.
11. J. Estes and G. Moddel, *Physical Review B* **1996**, 54, 14633.
12. V. A. Sivakov, F. Voigt, A. Berger, G. Bauer and. Bauer, S. H. Christiansen, *Physical Review B* **2010**, 82, 125446.
13. R. P. Prasankumar, P. C. Upadhya and A. J. Taylor, *Physica status solidi B* **2009**, 246, 1973.
14. T. Wang, B. Yu, Y. Liu, Q. Guo, Guo, K. Sheng and M. J. Deen, *Nanotechnology* **2012**, 23, 015307.

15. D. B. Kao, J. P. Mcvittie, W. D. Nix and K. C. Saraswat, *IEEE transactions on electron devices* **1998**, *ED-35*, 25.
16. R. P. Prasankumar, S. Choi, S. A. Trugman, S. T. Picraux and A. J. Taylor, *Nano Lett.* **2008**, *8*, 1619.
17. E. M. Grumstrup, M. M. Gabriel, E. M. Cating, C. W. Pinion, J. D. Christesen, J. R. Kirschbrown, E. L. Vallorz, J. F. Cahoon and J. M. Papanikolas, *J. Phys. Chem. C* **2014**, *118*, 8634.
18. W. J. Lee, J. W. Ma, J. M. Bae, M.-H. Cho and J. P. Ahn, *CrystEngComm.* **2011**, *13*, 690.
19. W. J. Lee, J. W. Ma, J. M. Bae, S. H. Park, K. S. Jeong, M.-H. Cho, C. Lee, K. J. Han and K. B. Jeong, *J. Mater. Chem.* **2012**, *22*, 19744.
20. J. M. Bae, W. J. Lee, J. W. Ma, M.-H. Cho, J. P. Ahn and H. S. Lee, *Nano Res.* **2012**, *5*, 152.
21. J. Faure, J. V. Tilborg, R. A. Kaindl and W. P. Leemans, *Optical and Quantum Electronics* **2004**, *36*, 681.
22. P. C. M. Planken, H. K. Nienhuys, H. J. Bakker and T. Wenckebach, *J. Opt. Soc. Am. B* **2001**, *18*, 313.
23. R. Q. Zhang, Y. Lifshitz, D. D. D. Ma, Y. L. Zhao, Th. Frauenheim, S. T. Lee, and S. Y. Tong, *J. Chem. Phys.* **2005**, *123*, 144703.
24. L. Seehofer, S. Huths, G. Falkenberg, and R. L. Johnson, *Surf. Sci.* **1995**, *329*, 157.
25. R. Hild, C. Seifert, M. Kammler, F.-J. Meyer zu Heringdorf, M. Horn-von Hoegen, R. A. Zhachuk, and B. Z. Olshanetsky, *Surf. Sci.* **2002**, *512*, 117.
26. H. Minoda, K. Yagi, F.-J. Meyer zu Heringdorf, Meier, D. Kaehler, and M.

- Horn-von Hoegen, *Phys. Rev. B* **1999**, *59*, 2363.
27. H. C. Jeong and E. D. Williams, *Surface Science Reports* **1999**, *34*, 171.
28. F. M. Ross, J. Tersoff, and M. C. Reuter, *Phys. Rev. Lett.* **2005**, *95*, 146104
29. Moutanabbir, S. Senz, R. Scholz, M. Alexe, Y. Kim, E. Pippel, Y. Wang, C. Wiethoff, T. Nabbefeld, F. Meyer zu Heringdorf and M. Horn-von Hoegen, *ACS Nano* **2011**, *5*, 1313.
30. Moutanabbir, D. Isheim, H. Blumtritt, S. Senz, E. Pippel and D. N. Seidman, *Nature* **2013**, *496*, 78.
31. W. J. Lee , J. W. Ma, J. M. Bae, M.-H. Cho, J. P. Ahn, *Mater. Res. Bull.* **2012**, *47*, 2739.
32. H. Z. Massoud, J. D. Plummer and E. A. Irene, *J. Electrochem. Soc.* **1985**, *132*, 2693.
33. F. Ma, S.C. Rustagi, G. S. Samudra, H. Zhao, N. Singh, G. Lo and D. Kwong, *Electron Device Letters, IEEE* **2010**, *31*, 719.
34. F. J. Himpsel, F. R. Mcfeely, A. T. Ibrahimi and J. A. Yarmoff, *Phys. Rev. B* **1988**, *38*, 6084.
35. H. Nishikawa, T. Shiroyama, R. Nakamura and Y. Ohki, *Phys. Rev. B* **1992**, *45*, 586.
36. A. Othonos, *J. Appl. Phys.* **1998**, *83*, 1789.
37. R. Calaro, M. Marso, T. Richter, I. A. Aykanat, R. Meijers, A. Hart, T. Stoica and H. Luth, *Nano Lett.* **2005**, *5*, 981.

Table

Table 1. Carrier decay times from OPTP measurements of Si NWs subjected to various oxidation times

Oxidation time [h]	d^2	τ_1 [ps]	τ_2 [ps]
0	6806	17.2	142.1
0.5	2070	34.1	144.4
1	784	34.0	152.0
2	216	33.5	155.6

Figure captions

Figure 1. (a) FE-SEM images of Au-etched Si NWs grown by the VLS method. (b) TEM images and the SAED pattern of as-grown Si NWs before removal of their Au tips. (c) Histogram of diameters of as-grown Si NWs. (d) TEM images of a Si NW oxidized for 2 h after removal of the Au tip.

Figure 2. TEM images illustrating the evolution of the cross-sectional shape of Si-core NWs with increasing oxidation time. (a–d) Evolution of the shape of Si NWs for an initial diameter of approximately 96 nm, at oxidation times (a) 0 min, (b) 30 min, (c) 1 h, and (d) 2 h. (e–h) Shape evolution for Si NWs of initial diameter approximately 75 nm, at oxidation times (e) 0 min, (f) 30 min, (g) 1 h, and (h) 2 h.

Figure 3. (a) Initial deposition of Si atoms from the supersaturated Au-Si alloy, forming the hexagonal shape. (b) Illustration of the 3-fold symmetrical hexagonal cross section of the Si core. (c, d) Distribution charts of Y/X extracted from a lot of Si NWs; the mean value of Y/X was 1.535 and the standard deviation was 0.068.

Figure 4. Illustration of the change in the cross-sectional shape of the Si core during the oxidation process, from (a) a 3-fold symmetrical hexagon into (b) a rounded triangle. After the thermal oxidation, the SiO₂ shell assumed the shape of the black circle depicted in (b), and the Si core shrank to the dark blue region depicted in (b).

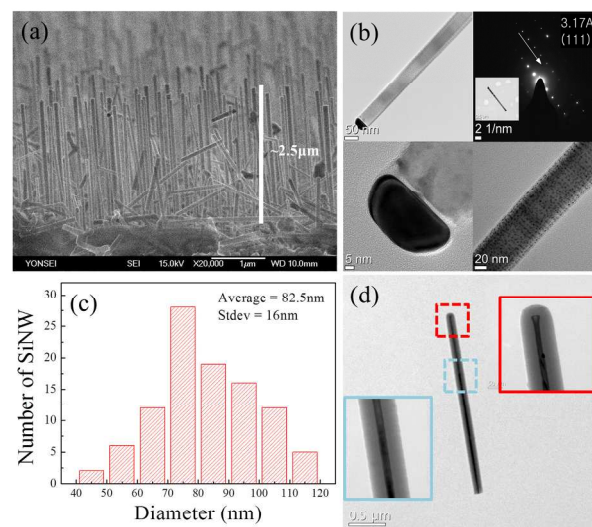
Figure 5. Schematic diagram of changes in the cross-sectional shape of Si-core NWs for

oxidation times up to 2 h. When oxidation was continued up to 9 h, the Si core disappeared altogether, leaving an oxide-only NW.

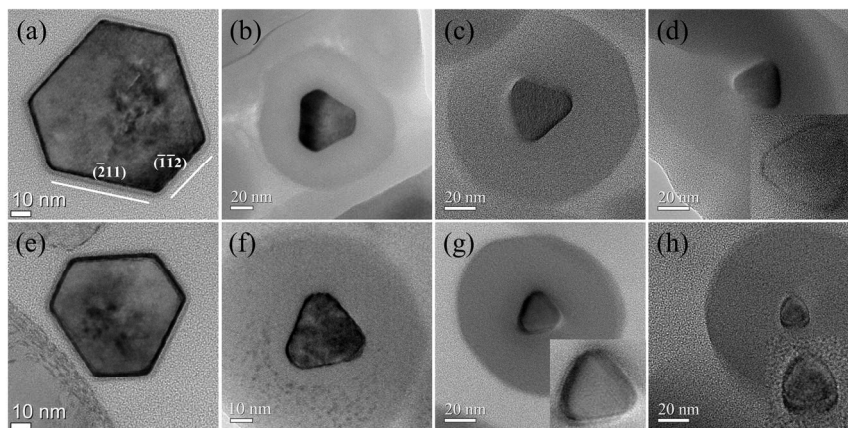
Figure 6. (a) Si core diameter and total diameter of Si/SiO₂ core/shell NWs versus oxidation time. (b) Quantitative volume of the SiO₂ shell and interfacial area between the Si core and the SiO₂ shell versus oxidation time.

Figure 7. (a) PL spectra measured at low-temperature of 7K from the oxidized Si NWs as a function of oxidation time. (b) The changing tendency of PL peak intensity near 400 nm as a function of oxidation time.

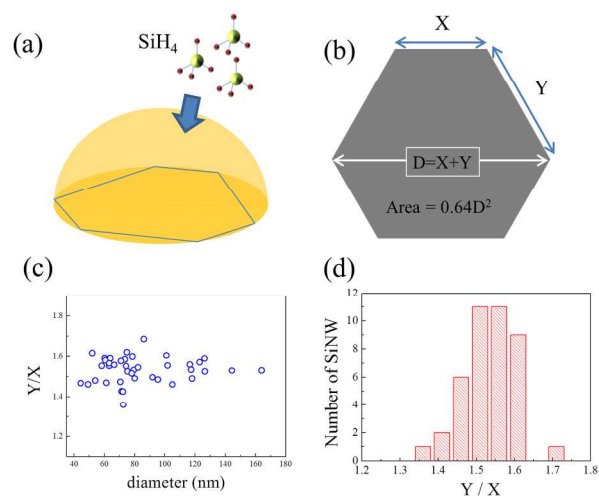
Figure 8. (a) Schematic diagram of the time-resolved THz spectrometer used in the optical-pump THz-probe experiments. (b) Normalized $\Delta T/T_0$ measured from Si NWs versus oxidation time.

Figure 1. Bae *et. al.*

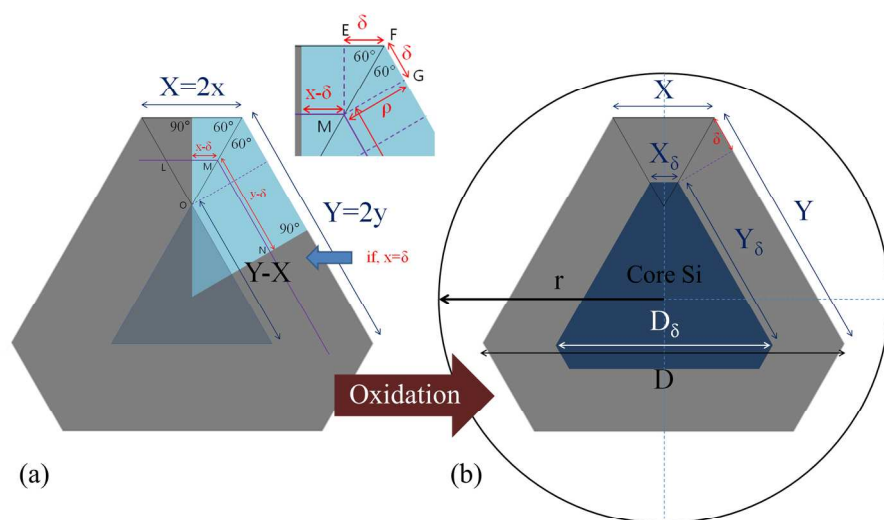
190x142mm (300 x 300 DPI)

Figure 2. Bae *et. al.*

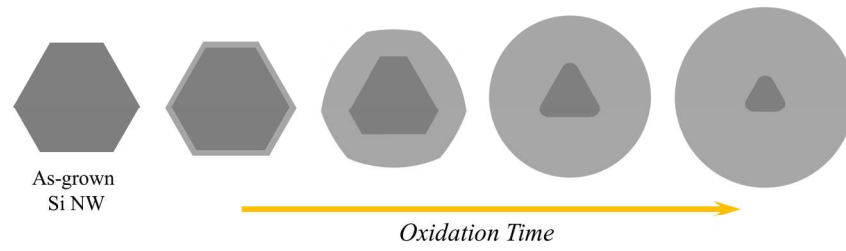
190x142mm (300 x 300 DPI)

Figure 3. Bae *et. al.*

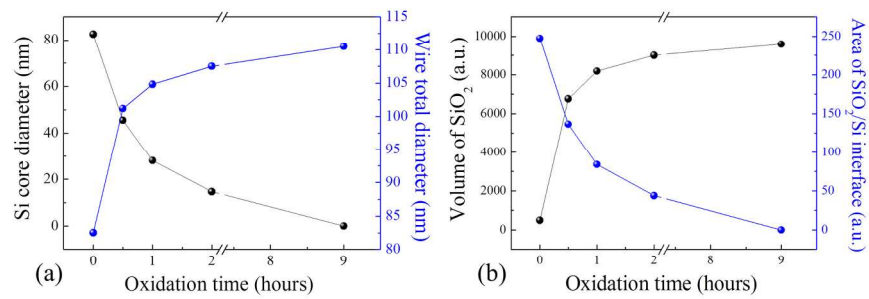
190x142mm (300 x 300 DPI)

Figure 4. Bae *et. al.*

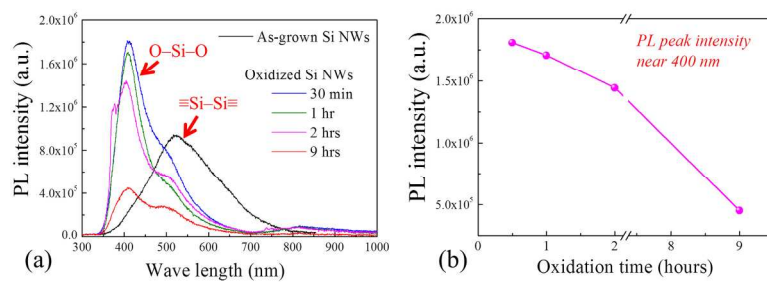
190x142mm (300 x 300 DPI)

Figure 5. Bae *et. al.*

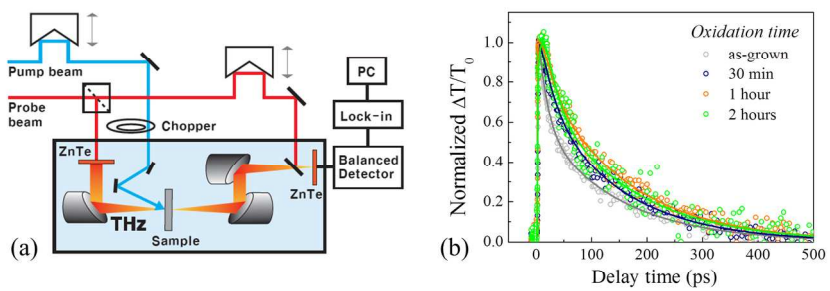
190x142mm (300 x 300 DPI)

Figure 6. Bae *et. al.*

190x142mm (300 x 300 DPI)

Figure 7. Bae *et. al.*

190x142mm (300 x 300 DPI)

Figure 8. Bae *et. al.*

190x142mm (300 x 300 DPI)